Article

Coupled InGaAs Quantum Dots for Electro-Optic Modulation

Kuei-Ya Chuang, Te-En Tzeng and Tsong-Sheng Lay *

Department of Electrical Engineering, Graduate Institute of Optoelectronic Engineering, National Chung Hsing University, Taichung City 402, Taiwan; m923050003@gmail.com (K.-Y.C.); Jeffreytzeng@gmail.com (T.-E.T.)
* Correspondence: tslay@dragon.nchu.edu.tw

Abstract: We investigated the growth of vertically coupled $In_{0.75}Ga_{0.25}As$ quantum dots (QDs) by varying the GaAs spacer thickness (d). Vertically-aligned triple-layer QDs of uniform size and highest accumulated strain are formed with d = 5 nm. The electroluminescence (EL) characteristics for $In_{0.75}Ga_{0.25}As$ QDs show an emission spectrum at optical wavelength (λ) of $1100-1300$ nm. The EL spectra exhibit the highest optical gain at λ ~ 1200 nm, and the narrowest FWHM = 151 nm of the sample with d = 5 nm at injection current = 20 mA. Fabry–Perot measurements at λ = 1515 nm of TE and TM polarizations were carried out to investigate the electro-optic modulation for a single-mode ridge waveguide consisting of vertically-coupled triple-layer $In_{0.75}Ga_{0.25}As$ QDs (d = 5 nm). The linear (r) and quadratic (s) electro-optic coefficients are $r = 2.99 \times 10^{-11}$ m/V and $s = 4.10 \times 10^{-17}$ m²/V² for TE polarization, and $r = 1.37 \times 10^{-11}$ m/V and $s = 3.2 \times 10^{-17}$ m²/V² for TM polarization, respectively. The results highlight the potential of TE/TM lightwave modulation by InGaAs QDs at photon energy below energy band resonance.

Keywords: quantum dots; electroluminescence; electro-optic effect; molecular beam epitaxy; InGaAs

1. Introduction

Self-assembled InGaAs quantum dots (QDs) grown on GaAs have been extensively explored for optoelectronic applications at optical wavelength (λ) = 1100–1300 nm. QD structures, which possess zero-dimensional carrier confinement, have demonstrated low threshold current, high characteristic temperature, and low chirp for the operations of diode lasers [1–3]. However, due to the low areal density and inhomogeneous size distribution, a single QDs layer provides limited advantage for optoelectronic device performance. Vertically-stacked multiple QDs layers are required to enhance the optical modal gain [4] to facilitate device applications such as semiconductor optical amplifiers [5] and photodetectors [6]. Since the InGaAs QDs are under compressive strain, spacer layers of 30–50 nm are often grown between the QDs layers to depress the strain accumulation and lattice defects. The rather thick spacer would hamper the electronic coupling between the QDs layers and reduce the dipole interaction between electron and photon. Close-stacking QDs multiple layers of rigorously reduced spacer layer thickness are expected to enhance the favorable optoelectronic characteristics, such as high modal gain and high oscillator strength. One of the approaches is depositing a short-period GaAs/InAs superlattice on top of a seed InAs QDs layer to form columnar quantum dots [7,8]. For each InAs/GaAs cycle in the superlattice, the InAs thickness is lower than the critical thickness, and the GaAs spacer thickness is only a few monolayers. The post-like nanostructures with high aspect ratio are formed after the deposition of GaAs/InAs superlattice. The structure provides not only the optical gain for transverse-electric (TE) mode (i.e., polarization along the in-plane direction), but also transverse-magnetic (TM) mode (i.e., polarization along the growth direction). On the other hand, two-layer InGaAs QDs separated by a nominally 10 nm thick GaAs spacer to form a quantum dot molecule have been studied to observe the strong quantum coupling and entangling of excitons in the individual QD [9–12]. The excitons, which can be coherently manipulated by laser beam in the quantum dot molecule,

represent quantum bits applicable in quantum computing processors. Moreover, multiple stacking QDs layers have been investigated for the implementations of intermediate-band solar cells (IBSC) [13–16] in green energy harvest.

Meanwhile, lightwave communications are the major device applications for III–V compound semiconductor nanostructures. In addition to optical transmitters, amplifiers and receivers, optical signal modulation is the key technology in optical fiber communication at λ = 1.4–1.6 μm. Two major modulation techniques, namely intensity modulation and phase modulation, are commonly adopted. Intensity modulation is based on optical absorption near the band gap controlled by quantum-confined Stark effect (QCSE), such as electro-absorption modulators (EAM) of quantum well structures [17,18]. Phase modulation using the change of refractive index (Δn) to modulate the phase of optical signal is governed by electro-optic effect. For electro-optic modulators (EOM), the photon energy of the signal is well below the energy band resonance, and no optical absorption is required. The III–V compound semiconductor bulk materials, such as GaAs and InP, exhibit lower EO coefficients, both of linear Pockels effect and quadratic Kerr effect, compared to the lithium niobate ($LiNbO_3$) counterpart. However, much less work on EO effect of InGaAs QDs has been reported [19–23].

Here, we report the growth of p-i-n diodes consisting of triple-layer $In_{0.75}Ga_{0.25}As$ QDs by changing the GaAs spacer thickness (d). Material properties for the triple-layer QDs are examined by transmission electron microscope (TEM) and X-ray diffraction (XRD). The optical emission characteristics are measured by electroluminescence (EL) spectroscopy at different injection currents. For the study of EO effect, a single-mode ridge-waveguide based on the triple-layer InGaAs QDs is fabricated to measure the phase retardation at λ = 1515 nm in TE and TM polarizations.

2. Epitaxial Growth

The p-i-n diodes consisting of triple-layer QDs were grown by molecular beam epitaxy (MBE) on (100) n^+-GaAs substrates, as shown in Figure 1. Arsenic valved cracker was used to supply As_4 flux at the cracking zone temperature of 640 °C. The As_4 beam equivalent pressure was 6×10^{-5} Torr. After removing the surface oxide, 0.5 m GaAs buffer layer and 0.5 m $Al_{0.5}Ga_{0.5}As$ layer were grown at a substrate temperature (T_s) of 645 °C measured by thermocouple. Both of the layers were n-type doped by Si at doping concentration of 2×10^{18} cm^{-3}. The i-layer active region consisted of triple-layer QDs sandwiched between 0.2 m GaAs. The self-assembled $In_{0.75}Ga_{0.25}As$ QDs were of 3.4 ML ($\approx$1.5 θ_c, θ_c = 2.3 ML: critical thickness) coverage grown at T_s = 520 °C. The QDs growth rate was of 0.1 ML/sec. After the growth of QDs, a 10 nm $In_{0.1}Ga_{0.9}As$ capping layer was directly grown on the QDs at the same T_s. Then, the T_s was raised to 645 °C for the growth of the GaAs spacer layer. The GaAs spacer thicknesses for the three samples were d = 40 nm, 20 nm, and 5 nm, respectively. After the deposition of QDs active region, p-$Al_{0.5}Ga_{0.5}As$ and GaAs contact layers were grown to finish the p-i-n epi-structure. A reference sample of $In_{0.75}Ga_{0.25}As$ QDs single-layer without capping was grown to measure the size distribution by using atomic force microscope (AFM). The average size was of diameter ~ 20 $\pm$ 5 nm, and height ~ 4 $\pm$ 1 nm for the $In_{0.75}Ga_{0.25}As$ QDs. The QDs configurations in the epi-structures were observed by transmission electron microscope (TEM). Figure 2 shows the cross-section bright field (BF) images for the QDs. For the d = 40 nm and 20 nm samples, the position of QDs is randomly located without any correlations. As the GaAs spacer decreases to d = 5 nm, the QDs in each layer are well aligned in the vertical direction (epitaxial direction), and the dot size is much more uniform. The areal density of each layer for the $In_{0.75}Ga_{0.25}As$ QDs was estimated from the TEM images. They are 2.8×10^{10} cm^{-2}, 3.7×10^{10} cm^{-2}, and 4.5×10^{10} cm^{-2} for d = 40 nm, 20 nm, and 5 nm, respectively. In the TEM images, two lens-shaped dark features are observed at the bottom and top of each QDs layer. The dark feature is attributive to indium segregation as the deposition of 10 nm thick $In_{0.1}Ga_{0.9}As$ capping layer is followed by GaAs spacer of high growth temperature (T_s = 645 °C). The presence of indium adatoms floating to the surface is normally observed in the growth

of III–V compound semiconductor heterostructures [24–27]. The nonuniform feature of indium distribution might suggest the possible existence of double QDs and/or columnar QDs in each 10 nm QDs layer. The intriguing material and optoelectronic characteristics are further investigated.
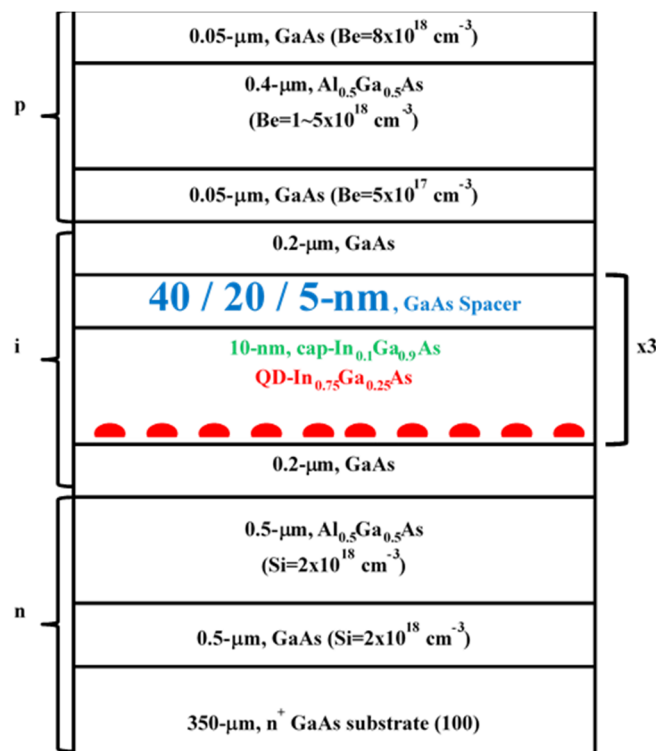
Figure 1. Schematic diagram of the p-i-n structure consisting of triple-layer $In_{0.75}Ga_{0.25}As$ QDs.
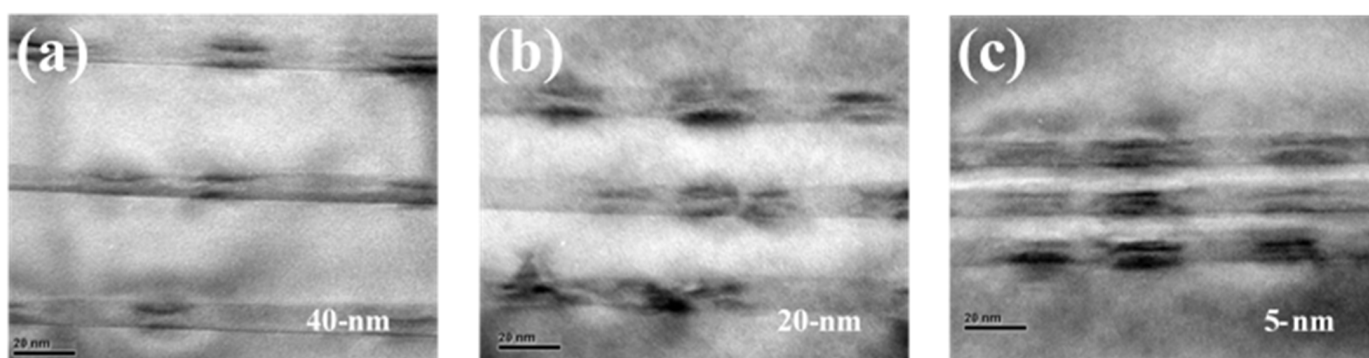
**Figure 2.** TEM cross-section BF images of the triple-layer $In_{0.75}Ga_{0.25}As$ QDs with (**a**) d = 40 nm, (**b**) d = 20 nm, and (**c**) d = 5 nm, respectively.

To investigate the formation of vertically aligned QDs, high-resolution $\omega/2\theta$ XRD scans across the (004) symmetric Bragg reflection were used to measure the effect of strain accumulation and lattice distortion for the QDs. The XRD data of the three samples are, respectively, shown in Figure 3. The X-ray wavelength is 1.54 Å and the Bragg angle (θ_B) of the GaAs substrate is 33.035°. For each sample, the XRD curve exhibits a maximum peak from the GaAs substrate, and periodic satellite peaks along the negative $\omega/2\theta$ axis. The periodic satellite peaks are from the triple-layer $In_{0.75}Ga_{0.25}As$ QDs. The increase of the periodicity for the satellite peaks is consistent with the decrease in GaAs spacer layer thickness from 40 nm to 5 nm. In addition, the position ($\Delta\theta$) of zero-order satellite peak

increases from –940 arcsec to –1600 arcsec against the decrease of GaAs spacer layer from 40 nm to 5 nm. We calculate the average perpendicular strain $<\varepsilon_\perp>$ given by [28]:

$$<\varepsilon_\perp> = \frac{\sin\theta_B}{\sin(\theta_B + \Delta\theta)} - 1 \tag{1}$$
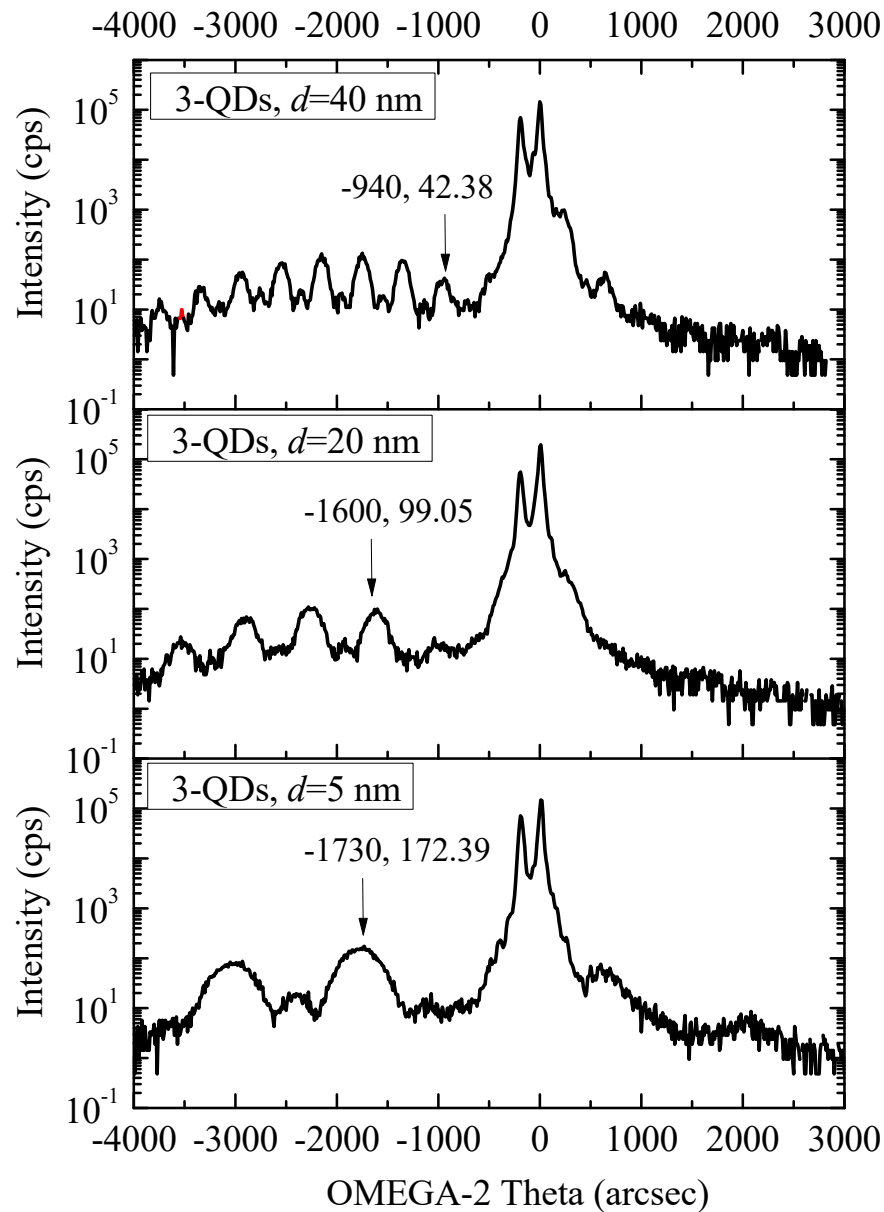
Figure 3. X-ray diffraction curves for the triple-layer $In_{0.75}Ga_{0.25}As$ QDs by varying GaAs spacer thickness with 40 nm, 20 nm, and 5 nm, respectively.

The experimental data is summarized in Table 1. The $<\varepsilon_\perp>$ increases from 0.00704 ($d = 40$ nm) to 0.01312 ($d = 5$ nm). The strain values indicate an 86% enhancement of compressive strain due to the closely packed QDs ($d = 5$ nm) of less strain relaxation. The enhancement of $<\varepsilon_\perp>$ in the $d = 5$ nm sample suggests that the formation of vertically-aligned QDs is similar to the growth of quantum dot lattice [29]. The bottom layer of QDs works as a seed layer. The strong compressive strain and high growth temperature ($T_s = 645\ ^\circ C$) of the GaAs spacer provide driving forces for indium adatoms diffusion towards the top of seed sites. The $<\varepsilon_\perp>$ data is also consistent with the full width at half-maximum (FWHM) of the zero-order satellite peak. A narrow FWHM = 170 arcsec for the

d = 40 nm sample attributed to a more uniform distribution of the vertical lattice constant, and less accumulated compressive strain of the epitaxial wafer. As the GaAs spacer layer thickness decreases to 20 nm and 5 nm, more compressive strain is accumulated, and the FWHM increases to 240 arcsec and 400 arcsec, respectively.

Table 1. XRD data including the FWHM and $\Delta\theta$ for the zero-order satellite peak, and the average perpendicular strain $<\varepsilon_\perp>$ for the triple-layer $In_{0.75}Ga_{0.25}As$ QDs of d = 40 nm, 20 nm, and 5 nm.

	d = 40 nm	d = 20 nm	d = 5 nm
FWHM (arcs)	170	240	400
$\Delta\theta$ (arcs)	−940	−1600	−1730
$<\varepsilon_\perp>$	0.0070	0.0121	0.0131

3. Electroluminescence Spectroscopy

Diodes of mesa structure were fabricated for the QDs samples to study the luminescence characteristics by electroluminescence (EL) spectroscopy. Figure 4 shows the room-temperature EL spectra of the triple-layer InGaAs QDs by varying the space layer thickness by 40, 20, and 5 nm, respectively. The EL spectra, which concentrate at optical wavelength (λ) ranging from 1100 nm to 1300 nm, confirm the optical emission from the QDs. As we increase the forward injection current from 2 mA to 20 mA, the EL spectra extend to shorter wavelengths, and the FWHM increases. The data indicates optical emission from higher subband transitions as more electron–hole pairs are injected. We normalized the EL spectra against the ground transition (S_0) near λ = 1300 nm, and the band-filling effect of the subband transition is observed as the injection current increases. The first subband transition (S_1) and second subband transition (S_2) are observed near λ = 1200 nm and 1160 nm, respectively. The major emission peak is near λ = 1200 nm, indicating the highest optical gain for the first subband transition (S_1). The observed energy separation between S_0 and S_1 peaks is ~48 meV both for d = 40 nm and 20 nm samples, while the energy separation increases to 66 meV for d = 5 nm sample. The increase of energy separation between S_0 and S_1 for the d = 5 nm sample indicates the enhancement of subband energy level separation by the exchange energy of interlayer tunnelling [30]. The FWHM of the whole EL spectrum is a qualified indicator to evaluate the size distribution and epitaxy homogeneity for the QDs. At 20 mA injection current, the FWHMs of the whole EL spectra are 262 nm, 213 nm, and 151 nm for d = 40 nm, 20 nm, and 5 nm, respectively. The EL results indicate a much more homogeneous size distribution for the triple-layer QDs with d = 5 nm, which is consistent with the data observed in material characterizations by TEM, and XRD.
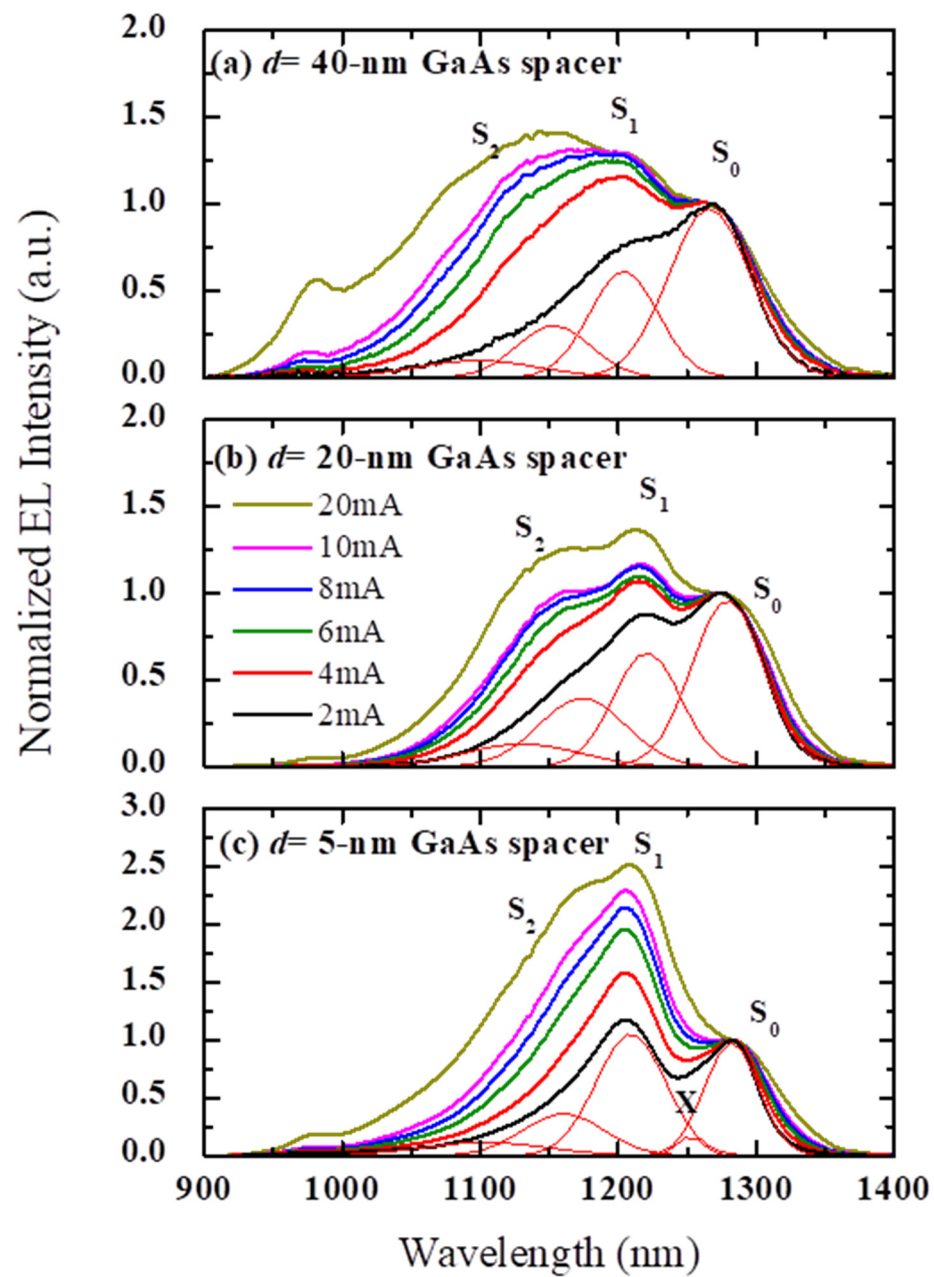
Figure 4. The normalized EL spectra for the p-i-n structure consisting of triple-layer $In_{0.75}Ga_{0.25}As$ QDs with (**a**) $d = 40$ nm, (**b**) $d = 20$ nm, and (**c**) $d = 5$ nm.

4. Electro-Optic Modulation

The wafer of triple-layer InGaAs QDs ($d = 5$ nm) was used to fabricate the ridge-waveguide EO modulator in view of the strong coupling between QDs and high accumulated strain field within the InGaAs QDs. Single-mode ridge waveguides of 2.2 μm width and 1 μm height were formed by ICP-RIE etching with $Ar/SiCl_4$ mixture gas. Therefore, the QDs active region is located within the ridge waveguide to ensure the optical signal is highly overlapped with the QDs. After the dry etching, 300 nm thick SiO_2 was deposited to protect the waveguides. The p-contact (Cr/Au) was realized on the waveguide surface by thermal evaporation. After p-contact deposition, the wafer was thinned down to 150 μm and the n-contact (Au/Ge/Au) was deposited on the substrate side. Figure 5a shows the schematic diagram of the single-mode ridge waveguide for the measurement of EO modulation. TE and TM optical mode profiles at $\lambda = 1515$ nm for the ridge waveguide were simulated. The TE mode profile is shown in Figure 5b. The intensity peaks of the TE and

TM modes are overlapped with the triple-layer QDs active region. The optical confinement factor (Γ) [31] is the fraction of the squared electric field confined to the triple-layer QDs active region. The Γ values of the TE and TM polarization are 0.07, and 0.061, respectively.
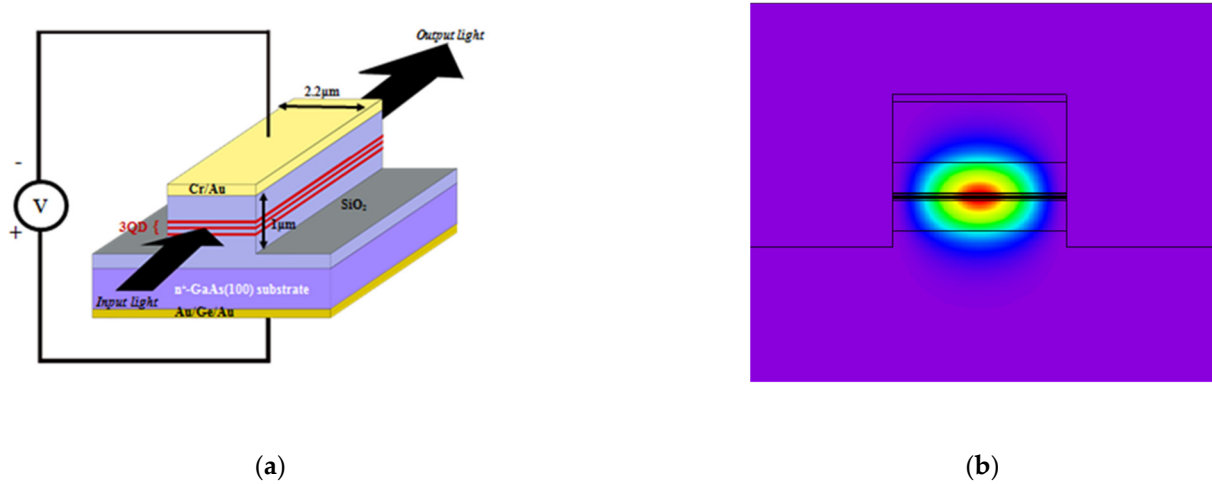
Figure 5. (**a**) Schematic diagram of EO measurement, and (**b**) TE mode profile at = 1515 nm for the single-mode ridge waveguide based on triple-layer $In_{0.75}Ga_{0.25}As$ QDs (*d* = 5 nm).

Fabry–Perot (FP) measurements near λ = 1515 nm were carried out by TE/TM polarized light from a tunable laser through the fiber polarization controller. The optical output at the end facet of a 1.52 mm long waveguide is collected by lens fiber and measured by photodetector. The applied electric field by reverse bias voltage is perpendicular to the epitaxy layers. The FP resonance fringes for TE and TM at different reverse bias are shown in Figure 6a,b, respectively. By applying voltage bias, the phase of the FP resonance fringes shift, indicating the change of refractive index (Δn) by EO effect. The phase retardation ($\Delta\Phi$) increases as we increase the reverse bias from 0 V to −4 V. From the wavelengths of the resonance peaks, we calculate the TE mode effective index n_{TE} = 3.367. Voltage-dependent phase shift is also observed for TM polarization, as shown in Figure 6b. The TM mode effective index n_{TM} is 3.355. We measured the phase shift of the Fabry–Perot resonance under reverse-bias voltages. The index change is related to the phase shift given by [20]:

$$\Delta\phi = \pi L n_0^3 \Gamma (r \cdot E + s \cdot E^2)$$

$$\Delta n = \Delta\phi\ \lambda\ /\ 2\pi L \tag{2}$$

where L is the waveguide length, n_0 is the effective refractive index, *E* is the electric field applied in the active region, *r* and *s* are the linear and quadratic electro-optic coefficients, respectively, and Γ is the confinement factor. At λ = 1515 nm and voltage bias = −4 V, we obtain $\Delta\phi$ = 96.4°/mm and $\Delta n = 4.06 \times 10^{-4}$ for TE polarization, and $\Delta\phi$ = 74.8°/mm and $\Delta n = 3.16 \times 10^{-4}$ for TM polarization, respectively.

The phase retardation and refractive index change as a function of reverse bias, as shown in Figure 7. The linear (Pockels) and quadratic (Kerr) electro-optic coefficients are extracted according to Equation (2). For the data of TE polarization shown in Figure 7a, the linear (*r*) and quadratic (*s*) electro-optic coefficient are $r = 2.99 \times 10^{-11}$ m/V and $s = 4.10 \times 10^{-17}$ m^2/V^2, respectively. For TM polarization shown in Figure 7b, electro-optic coefficient $r = 1.37 \times 10^{-11}$ m/V and $s = 3.2 \times 10^{-17}$ m^2/V^2 are extracted. The electro-optic coefficients are comparable to $r = 3.1 \times 10^{-11}$ m/V for $LiNbO_3$ electro-optic modulators and InAs quantum dot waveguides [19–23], and larger than bulk GaAs material and InGaAs-based multiple quantum wells at λ ~ 1500 nm [32,33].
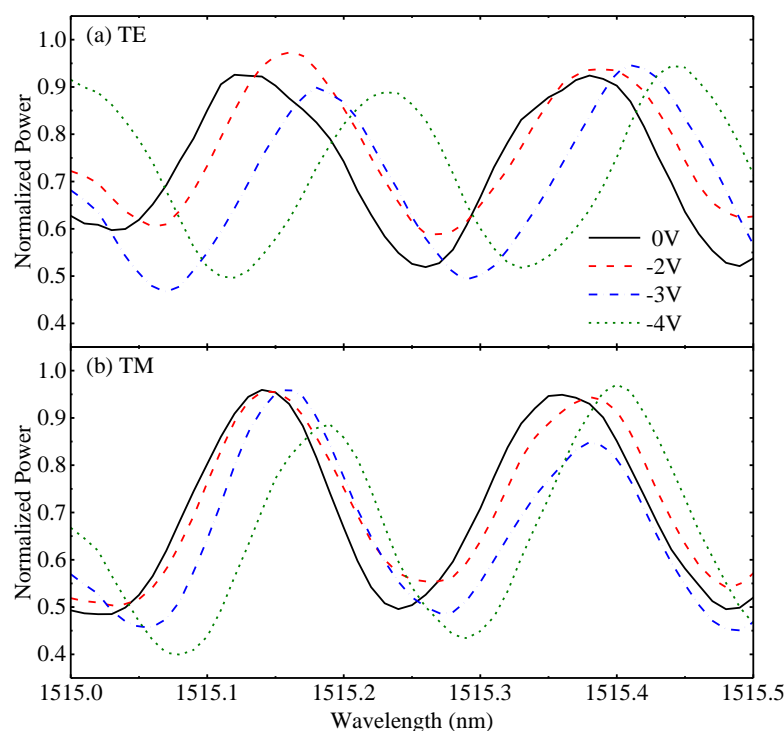
Figure 6. Phase shifts of the Fabry–Perot resonances at reverse bias voltages for (**a**) TE and (**b**) TM polarization.
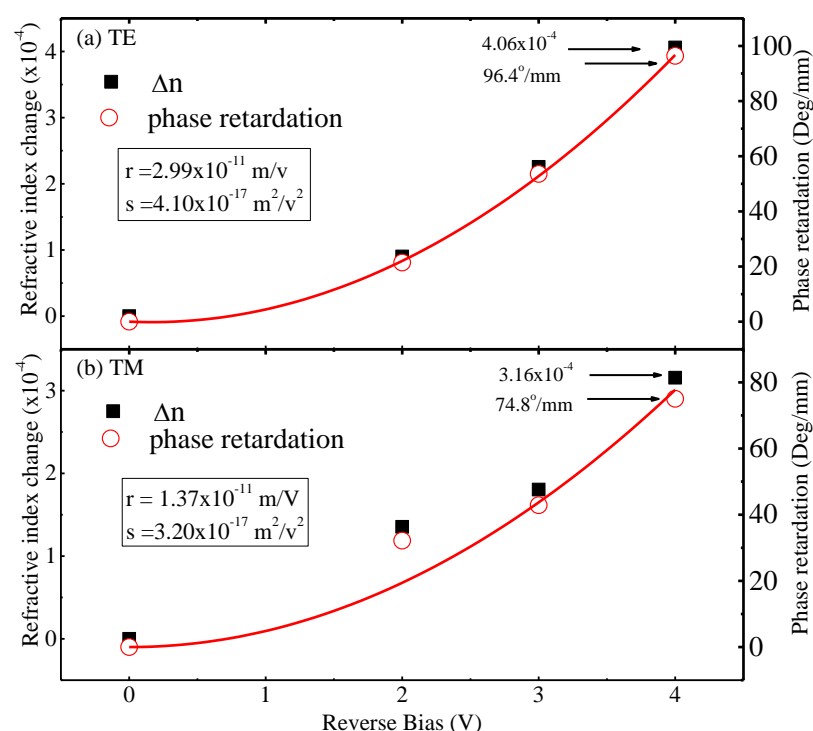
Figure 7. Phase retardation ($\Delta\phi$) and refractive index change (Δn) as a function of reverse bias voltages for (**a**) TE and (**b**) TM polarization. The curve is a fit to the $\Delta\phi$ data to extract EO linear coefficient (*r*) and quadratic coefficient (*s*).

5. Conclusions

Triple-layer In$_{0.75}$Ga$_{0.25}$As QDs structures were grown by varying the GaAs spacer thickness of 40 nm, 20 nm, and 5 nm, respectively. Vertically-aligned QDs formation and homogeneous distribution of QD size and position were observed for the sample

of d = 5 nm. The results are attributed to the higher strain accumulation, as shown in XRD data. The optical emission characteristics for the triple-layer $In_{0.75}Ga_{0.25}As$ QDs were measured by electroluminescence spectroscopy. The EL spectra concentrated at λ = 1100–1300 nm. As injection current increases, the emission spectra are extended to shorter wavelengths by subband filling effect for the QDs. The EL spectrum shows the narrowest FWHM = 151 nm for the triple-layer $In_{0.75}Ga_{0.25}As$ QDs with d = 5 nm. The data indicates a homogeneous QD size distribution for the d = 5 nm sample, which is consistent with the TEM and XRD results. A single-mode ridge waveguide consisting of the triple-layer $In_{0.75}Ga_{0.25}As$ QDs (d = 5 nm) was fabricated to measure the electro-optic coefficients both in TE and TM polarizations. The linear (r) and quadratic (s) electro-optic coefficients at λ = 1515 nm are $r = 2.99 \times 10^{-11}$ m/V and $s = 4.10 \times 10^{-17}$ m^2/V^2 for TE polarization, and $r = 1.37 \times 10^{-11}$ m/V and $s = 3.2 \times 10^{-17}$ m^2/V^2 for TM polarization, respectively. The results are comparable to $LiNbO_3$ electro-optic modulators, and highlight the potential of TE/TM lightwave modulation by InGaAs QDs at photon energy below energy band resonance.

Author Contributions: Conceptualization, T.-S.L.; Data curation, T.-S.L.; Investigation, K.-Y.C. and T.-E.T. All authors have read and agreed to the published version of the manuscript.

Data Availability Statement: Not applicable.

Conflicts of Interest: The authors declare no conflict of interest.

References

1. Schafer, F.; Reithmaier, J.P.; Forchel, A. High-performance GaInAs/GaAs quantum-dot lasers based on a single active layer. *Appl. Phys. Lett.* **1999**, *74*, 2915–2917. [CrossRef]
2. Liu, G.T.; Stintz, A.; Li, H.; Malloy, K.J.; Lester, L.F. Extremely low room-temperature threshold current density diode lasers using InAs dots in $In_{0.15}Ga_{0.85}$ As quantum well. *Electron. Lett.* **1999**, *35*, 1163–1164. [CrossRef]
3. Novikov, I.I.; Gordeev, N.Y.; Karachinski, L.Y.; Maksimov, M.V.; Shernyakov, Y.M.; Kovsh, A.R.; Krestnikov, I.L.; Kozhukhov, A.V.; Mikhrin, S.S.; Ledentsov, N.N. Effect of p-doping of the active region on the temperature stability of InAs/GaAs QD lasers. *Semiconductors* **2005**, *39*, 477–480. [CrossRef]
4. Martinez, A.; Lemaitre, A.; Merghem, K.; Ferlazzo, L.; Dupuis, C.; Ramdane, A.; Provost, J.G.; Dagens, B.; Le Gouezigou, O.; Gauthier-Lafaye, O. Static and dynamic measurements of the α-factor of five-quantum-dot-layer single-mode lasers emitting at 1.3 μm on GaAs. *Appl. Phys. Lett.* **2005**, *86*, 211115. [CrossRef]
5. Nielsen, D.; Chuang, S.L.; Lee, D.; Kim, N.J.; Pyun, S.H.; Jeong, W.G.; Chen, C.Y.; Lay, T.S. High-speed wavelength conversion in quantum dot and quantum well semiconductor optical amplifiers. *Appl. Phys. Lett.* **2008**, *92*, 211101. [CrossRef]
6. Kim, S.M.; Harris, J.S. Multicolor InGaAs quantum-dot infrared photodetectors. *IEEE Photon. Technol. Lett.* **2004**, *16*, 2538–2540. [CrossRef]
7. Ridha, P.; Li, L.; Fiore, A.; Patriarche, G.; Mexis, M.; Smowton, P.M. Polarization dependence study of electroluminescence and absorption from InAs/GaAs columnar quantum dots. *Appl. Phys. Lett.* **2007**, *91*, 191123. [CrossRef]
8. He, J.; Krenner, H.J.; Pryor, C.; Zhang, J.P.; Wu, Y.; Allen, D.G.; Morris, C.M.; Sherwin, M.S.; Petroff, P.M. Growth, structural, and optical properties of self-assembled (In,Ga) As quantum posts on GaAs. *Nano Lett.* **2007**, *7*, 802–806. [CrossRef]
9. Bayer, M.; Hawrylak, P.; Hinzer, K.; Fafard, S.; Korkusinski, M.; Wasilewski, Z.R.; Stern, O.; Forchel, A. Coupling and entangling of quantum states in quantum dot molecules. *Science* **2001**, *291*, 451–453. [CrossRef]
10. Krenner, H.J.; Sabathil, M.; Clark, E.C.; Kress, A.; Schuh, D.; Bichler, M.; Abstreiter, G.; Finley, J.J. Direct observation of controlled coupling in an individual quantum dot molecule. *Phys. Rev. Lett.* **2005**, *94*, 057402. [CrossRef]
11. Stinaff, E.A.; Scheibner, M.; Bracker, A.S.; Ponomarev, I.V.; Korenev, V.L.; Ware, M.E.; Doty, M.F.; Reinecke, T.L.; Gammon, D. Optical signatures of coupled quantum dots. *Science* **2007**, *317*, 929–932. [CrossRef] [PubMed]
12. Xu, X.; Sun, B.; Berman, P.R.; Steel, D.G.; Bracker, A.S.; Gammon, D.; Sham, L.J. Coherent optical spectroscopy of a strongly driven quantum dot. *Science* **2006**, *311*, 636–639. [CrossRef] [PubMed]
13. Hirao, K.; Asahi, S.; Kaizu, T.; Kita, T. Two-step photocurrent generation enhanced by the fundamental-state miniband formation in intermediate-band solar cells using highly homogeneous InAs/GaAs quantum-dot superlattice. *Appl. Phys. Rev.* **2017**, *11*, 012301. [CrossRef]
14. Okada, Y.; Ekins-Daukes, N.J.; Kita, T.; Tamaki, R.; Yoshida, M.; Pusch, A.; Hess, O.; Phillips, C.C.; Farrell, D.J.; Yoshida, K.; et al. Intermediate band solar cells: Recent progress and future directions. *Appl. Phys. Rev.* **2015**, *2*, 021302. [CrossRef]

15. Tasco, V.; Arianna, C.; Taurino, A.; Cola, A.; Catalano, M.; Salhi, A.; Che, Z.; Kim, M.J.; Lomascolo, M.; Passaseo, A. Inter-level carrier dynamics and photocurrent generation in large band gap quantum dot solar cell by multistep growth. *Sol. Energy Mater. Sol. Cells* **2017**, *171*, 142–147. [CrossRef]

16. Lay, T.S.; Lin, Z.H.; Chuang, K.Y.; Tzeng, T.E. InGaAs quantum dots-in-a-well solar cells with anti-reflection coating. *J. Cryst. Growth* **2019**, *513*, 6–9. [CrossRef]

17. Miller, D.A.B.; Chemla, D.S.; Damen, T.C.; Gossard, A.C.; Wiegmann, W.; Wood, T.H.; Burrus, C.A. Electric field dependence of optical absorption near the band gap of quantum-well structures. *Phys. Rev. B* **1985**, *32*, 1043–1060. [CrossRef]

18. Amin, R.; Khurgin, J.B.; Sorger, V.J. Waveguide-based electro-absorption modulator performance: Comparative analysis. *Opt. Express* **2018**, *26*, 15445–15470. [CrossRef]

19. Qasaimeh, O.; Kamath, K.; Bhattacharya, P.; Phillips, J. Linear and quadratic electro-optic coefficients of self-organized $In_{0.4}Ga_{0.6}As$/GaAs quantum dots. *Appl. Phys. Lett.* **1998**, *72*, 1275–1277. [CrossRef]

20. Gosh, S.; Lenihan, A.S.; Dutt, M.V.G.; Qasaimeh, O.; Steel, D.G.; Bhattacharya, P. Nonlinear optical and electro-optic properties of InAs/GaAs self-organized quantum dots. *J. Vac. Sci. Technol. B* **2001**, *19*, 1455–1458. [CrossRef]

21. Moreau, G.; Martinez, A.; Cong, D.Y.; Merghem, K.; Miard, A.; Lemaitre, A.; Voisin, P.; Ramdane, A.; Krestnikov, I.; Kovsh, A.R.; et al. Enhanced In(Ga)As/GaAs quantum dot based electro-optic modulation at 1.55 μm. *Appl. Phys. Lett.* **2007**, *91*, 091118. [CrossRef]

22. Shin, J.; Kim, H.; Petroff, P.M.; Dagli, N. Enhanced electro-optic phase modulation in InGaAs quantum posts at 1500nm. *IEEE J. Quantum Electron.* **2010**, *46*, 1127–1131. [CrossRef]

23. Akca, I.B.; Dana, A.; Aydinli, A.; Rossetti, M.; Li, L.; Fiore, A.; Dagli, N. Electro-optic and electro-absorption characterization of InAs quantum dot waveguides. *Opt. Express* **2008**, *16*, 3439–3444. [CrossRef]

24. Taurino, A.; Catalano, M.; De Giorgi, M.; Passaseo, A.; Cingolani, R. Effects of coupling on the structural properties of $In_xGa_{1-x}As$/GaAs 1-D and 0-D self-organized quantum structures. *Mater. Sci. Eng.* **2001**, *B87*, 256–261. [CrossRef]

25. Moison, J.M.; Guille, C.; Houzay, F.; Barthe, F.; Van Rompay, M. Surface segregation of third-column atoms in group III-V arsenide compounds: Ternary alloys and heterostructures. *Phys. Rev. B* **1989**, *40*, 6149–6162. [CrossRef]

26. Howe, P.; Le Ru, E.C.; Clarke, E.; Murray, R.; Jones, T.S. Quantification of segregation and strain effects in InAs/GaAs quantum dot growth. *J. Appl. Phys.* **2005**, *98*, 113511. [CrossRef]

27. Krost, A.; Heinrichsdorff, F.; Bimberg, D. High-resolution x-ray diffraction of self-organized InGaAs/GaAs quantum dot structures. *Appl. Phys. Lett.* **1996**, *68*, 785–787. [CrossRef]

28. Nuntawong, N.; Birudavolu, S.; Hains, C.P.; Huang, S.; Xu, H.; Huffaker, D.L. Effect of strain-compensation in stacked 1.3 μm InAs/GaAs quantum dot active regions grown by metalorganic chemical vapor deposition. *Appl. Phys. Lett.* **2004**, *85*, 3050–3052. [CrossRef]

29. Gerardot, B.D.; Subramanian, G.; Minvielle, S.; Lee, H.; Johnson, J.A.; Schoenfeld, W.V.; Pine, D.; Speck, J.S.; Petroff, P.M. Self-assembling quantum dot lattices through nucleation site engineering. *J. Cryst. Growth* **2002**, *236*, 647–654. [CrossRef]

30. Lay, T.S.; Ying, X.; Shayegan, M. Layer-depopulation- and magnetic-field-induced resistance oscillations in a triple-layer electron system. *Phys. Rev. B* **1995**, *52*, R5511–R5514. [CrossRef]

31. Huang, Y.H.; Pan, Z.; Wu, R.H. Analysis of the optical confinement factor in semiconductor lasers. *J. Appl. Phys.* **1996**, *79*, 3827–3830. [CrossRef]

32. Berseth, C.A.; Wuethrich, C.; Reinhart, F.K. The electro-optic coefficients of GaAs: Measurements at 1.32 and 1.52 μm and study of their dispersion between 0.9 and 10 μm. *J. Appl. Phys.* **1992**, *71*, 2821–2825. [CrossRef]

33. Nishimura, S.; Inoue, H.; Sano, H.; Ishida, K. Electrooptic effects in an InGaAs/InAlAs multiquantum well structure. *IEEE Photon. Technol. Lett.* **1992**, *4*, 1123–1126. [CrossRef]